Soft Matter

PAPER

View Article Online
View Journal | View Issue

Cite this: *Soft Matter*, 2019, **15**, 989

Spherical-cap droplets of a photo-responsive bent liquid crystal dimer†

Jun Yoshioka,[a] Péter Salamon,[b] Daniel A. Paterson,[c] John M. D. Storey,[c] Corrie T. Imrie,[c] Antal Jákli,[d] Fumito Araoka*[a] and Agnes Buka*[b]

Received 26th August 2018,
Accepted 8th January 2019

DOI: 10.1039/c8sm01751d

rsc.li/soft-matter-journal

Using a photo-responsive dimer exhibiting the transition between nematic (N) and twist-bend nematic (N_{TB}) phases, we prepared spherical cap-shaped droplets on solid substrates exposed to air. The internal director structures of these droplets vary depending on the phase and on the imposed boundary conditions. The structural switching between the N and N_{TB} phases was successfully performed either by temperature control or by UV light-irradiation. The N phase is characterized by an extremely small bend elastic constant K_3, and surprisingly, we found that the droplet–air interface induces a planar alignment, in contrast to that seen for typical calamitic liquid crystals. As a consequence, the director configuration was stabilized in a structure substantially different from that normally found in conventional nematic liquid crystalline droplets. In the twist-bend nematic droplets characteristic structures with macroscopic length scales were formed, and they were well controlled by the droplet size. These results indicated that a continuum theory is effective in describing the stabilization mechanism of the macroscopic structure even in the twist-bend nematic liquid crystal droplets exhibiting director modulations on a scale of several molecular lengths.

I. Introduction

In liquid crystals (LCs) bounded by curved interfaces, geometrical frustrations play an important role in the formation of various topological states. For example, it is well-known that nematic (N) materials show unique structures in a spherical droplet or shell geometry bounded by an interface with a certain anchoring condition, because a geometrical frustration occurs in such a spherically confined state.[1–15] Spherical-cap geometries, such as a N LC droplet placed on a flat solid substrate, are a little more complicated, because the N LC is now surrounded by two different boundary conditions.[16] Here, it should be noted that strong anchoring is not always a prerequisite to induce the geometrical frustration.[15–19] For instance, a line defect is formed in the spherical-cap NLC droplet sandwiched by the substrate with planar anchoring and air interface with weak homeotropic anchoring, while such a defect is not constructed in the droplet on the substrate with homeotropic anchoring.[16] This indicates that rather than the anchoring strength, the combination of the anchoring condition and the shape of the boundary is essential to induce the geometrical frustration in the droplet.

In addition to the boundary conditions, elastic anisotropy also plays an important role. For example, spherical droplets with planar anchoring often exhibit the so-called 'bipolar' state, in which the N director field has two surface point defects. On the other hand, it can be transferred into the so-called 'axial' state with a central line defect, depending on the ratio of splay and bend elastic constants.[3,5] In addition, weak twist and bend elasticity (low twist and bend elastic constant) allows the system to be twist-preferred. Helix formation through the spontaneous twist deformation has been well-known even in N LCs of achiral molecules.[6–10]

Cholesteric (Ch), smectic (Sm), or columnar (Col) LC systems with curved boundaries are more complicated,[20–37] because the director structures are dominated not only by the two factors described already but also by others, such as helix formation due to the chirality or the compression elasticity due to the translational ordering with molecular length scales. The key point to be noticed here is the role played by frustration among these factors. For instance, spherical Ch droplets show multi-dimensional twists even without the aid of surface anchoring.[20–22] In other words, the use of anchoring may cause additional frustrations by which various complex topological states are realized in such droplets.[1,23–30] In this sense, LC materials showing the recently-found twist-bend nematic (N_{TB}) phase are attractive systems to study complex frustrations induced by the curved surface. The N_{TB} phase is characterised by spontaneous

[a] *RIKEN Center for Emergent Matter Science (CEMS), 2-1 Hirosawa, Wako, Saitama 351-0198, Japan*
[b] *Institute for Solid State Physics and Optics, Wigner Research Centre for Physics, Hungarian Academy of Sciences (HAS), H-1525 Budapest, P.O.B. 49, Hungary*
[c] *Department of Chemistry, School of Natural and Computing Sciences, University of Aberdeen, Meston Building, Old Aberdeen AB24 3UE, UK*
[d] *Chemical Physics Interdisciplinary Program, Liquid Crystal Institute, Kent State University, Kent, OH 44242-0001, USA*

† Electronic supplementary information (ESI) available. See DOI: 10.1039/c8sm01751d

twist and bend deformations due to the nanoscale heliconical structure,[38–57] which theoretically can be treated in the framework of a course-grained description.[38,40,45,46,48,49,52,53]

This paper focuses on the internal structures of spherical-cap droplets formed by a photoresponsive bent-dimer that exhibits the N–N_{TB} phase transition. In general, the N phases of such bent-dimers are characterized by extremely small bend elastic constants.[39–42] In addition, the LC–air interface of the present dimer system shows planar anchoring, in contrast to the majority of conventional calamitic N systems, for which the alignment is normal to the air interface. Thus, we can expect that these unique physical properties, *i.e.* the elastic anisotropy and the boundary conditions of this dimer, may induce a unique frustration in the structure of the droplets. In contrast to the previous studies dealing with the smectic-like bâtonnets in the coexisting state between the N–N_{TB} phase transition,[56,57] this paper pays particular attention to the spherical-cap geometry in both phases with two different interfacial conditions, one at the flat substrate and the other air. An additional feature of note in the present study is the photo-responsiveness due to the azobenzene moiety, which allows a photo-induced N_{TB}–N transition to be driven by ultraviolet (UV) light irradiation.[55] Here we also demonstrate the dynamic structure variation during the transition between the N and N_{TB} phases.

II. Experimental

A. Sample preparation

The bent-dimer we used, CB6OABOBu,[55] shows a direct transition from N to N_{TB} phase on cooling, and *vice versa* on heating. Since the N phase of this material appears in a relatively high temperature region (Cr 103 °C N_{TB} 105 °C N 157 °C Iso), we mixed the dimer with a conventional room temperature N LC (5CB, Tokyo Chemical Industry Co., Ltd) to lower the transition temperature between N and N_{TB}.[47,51] A sample mixture of 70% CB6OABOBu by weight fraction yielded the phase sequence, Cr-70 °C–N_{TB}-73 °C–N-120 °C-Isotropic (Iso), which was used in the present study. Critically, the photo-induced transition is possible even in the 70–30% mixture.

As for the droplet fabrication, 1–2 microliters chloroform solution with 0.1 wt% sample mixture content was cast on a glass substrate, followed by subsequent drying at above 100 °C for about 1 hour to completely remove the chloroform. Due to this evaporation process, micron-sized spherical-cap droplets are spontaneously formed on the substrate. Since the topological structure of the spherical-cap droplets depends on the anchoring of the substrate surface, we prepared three types of substrates: (i) bare glass (washed by sonication in an alkaline detergent and rinsed several times with pure water); (ii) unidirectionally rubbed glass coated with polyvinyl alcohol (rubbed-PVA, Aldrich), and (iii) non-rubbed glass coated with polyimide (JALS204, JSR Corp.). In typical calamitic liquid crystals, strong planar anchoring is induced at the PVA-coated substrate, whereas homeotropic is obtained at the substrate coated with JALS204 (Homeotropic PI).

B. Polarizing microscopy and optical simulation

The textures of the droplets were observed by polarizing microscopy (POM) using a commercial microscope (BH2, Olympus) and a digital camera (EOS Kiss X50, Canon). The observations were performed not only with crossed polarizers but also with an additional tint plate (retardation λ = 530 nm) for sensitive colour observation. Temperature control was achieved using a custom-made hot-stage, while the temperature inside the droplets was estimated to be lower than that in the stage because the present system was exposed to the air. In fact, the N–N_{TB} transition occurred when the temperature in the stage was 15–25 degrees higher than the transition temperature.

Based on the POM images we simulated the internal director fields using the Jones matrix method.[58] Spectral transmittances were calculated for 22 different wavelengths, and then converted into RGB values using the colour-matching function. The incident light was assumed to be a flat white light having an equal intensity over the calculated wavelength range. The ordinary refractive index n_o was assumed to be 1.5 according to ref. 59. A commercial spectroscope (USB2000+VIS-NIR, Ocean Optics) was used to obtain the extraordinary refractive index n_e[60] and the birefringence $\Delta n = n_e - n_o$. A mercury lamp (U-LH100HG equipped on BX53W, Olympus) was used for the *in situ* observation of the photo-induced phase transition under UV irradiation.

C. Confocal reflection microscopy (CRM)

A confocal reflection microscope (TCS SP8, Leica) was used to estimate the height of the spherical-cap droplets. We used a dry objective lens with a numerical aperture of 0.7, which corresponds to a focal depth of about 2.4 μm for the optical wavelength of 500 nm. The excitation and observation were made on the LC–air interface of the spherical-cap droplets. CRM analyses were carried out to measure the heights and contact angles of these droplets. Fig. 1(a)–(d) is an example of the CRM observations, showing the clear reflections at the substrate–air and LC–air interfaces, by which we could confirm the spherical-cap shape of the droplets. The droplet height h estimated from the cross-sectional CRM profile was plotted as a function of the radius R. As shown in Fig. 1(e), h is almost proportional to R, irrespective of surface treatment and observed phases. Thus, by assuming linearity between them, we can describe the contact angle θ_c as,

$$\theta_c = 2\arctan\left(\frac{h}{R}\right). \quad (1)$$

θ_c values deduced from the CRM data with the $\theta/2$ method[61] are summarized in Table 1. The contact angle depends strongly on the surface treatment of the glass: the angle was found to be largest for the homeotropic PI, and smallest for the rubbed PVA. From this result, the ratio of the surface energies of $(\gamma_{AS} - \gamma_{LS})/\gamma_{AL}$ is also calculated by the Young's equation, where γ_{AS}, γ_{LS} and γ_{AL} are the energies of air–substrate, LC–substrate, and air–LC interfaces, respectively. In all cases, since γ_{AL} would show similar values, the differences in θ_c should be attributed to those of $\gamma_{AS} - \gamma_{LS}$ in each substrate.

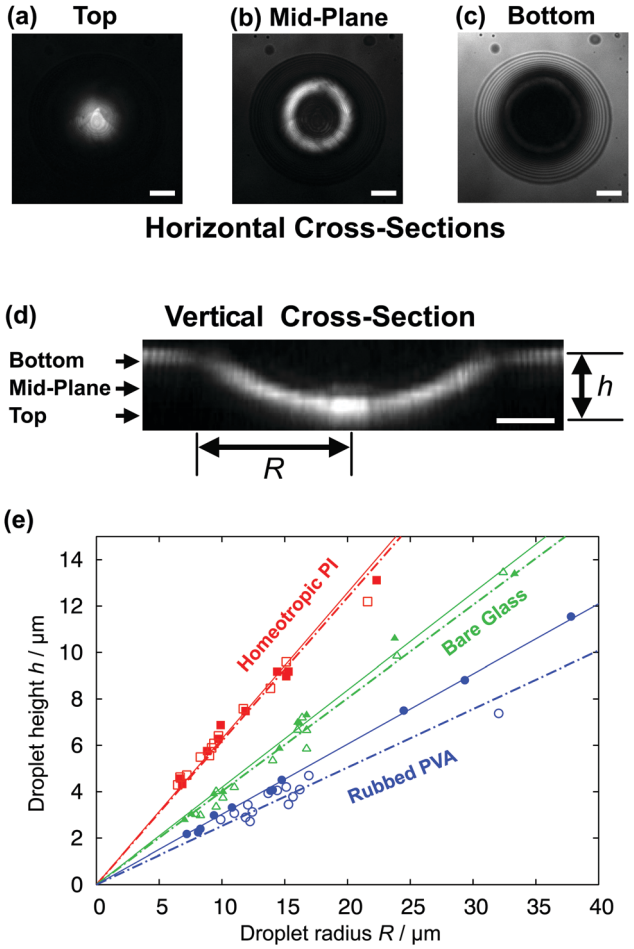

Fig. 1 (a–d) Example of CRM images of the spherical-cap N_{TB} droplet placed on the bare glass substrate ($T \sim 60$ °C). Scale bars, 10 μm. (a–c) Horizontal cross-sectional images taken for three different planes as described in (d). (d) Vertical cross-sectional image sliced at the centre, constructed from the horizontal cross-sectional images obtained by vertical scanning CFM. (e) The droplet height h plotted as a function of the droplet radius R. Both h and R are estimated from the vertical cross-section sliced at the centre, as shown in (e). Closed and open symbols are for N and N_{TB} droplets, respectively. Solid and dashed lines represent linear-fitting to them. Rectangles, triangles, and circles denote the homeotropic PI, the bare glass, and the rubbed PVA substrates, respectively. The temperature was ~90 °C for N and ~60 °C for N_{TB} droplets. See also the summary of the slope values h/R, from which the contact angle θ_c can be deduced.

Table 1 Summary of the shape-dependent parameters, height–radius ratio h/R, contact angle θ_c, and pitch–radius ratio of the stripe domains d/R, of the N and N_{TB} droplets. The ratio of the surface energies is obtained by the Young's equation, $\gamma_{AS} = \gamma_{LS} + \gamma_{AL}\cos\theta_c$, where γ_{AS}, γ_{LS} and γ_{AL} are the energies of air–substrate, LC–substrate, and air–LC interfaces, respectively

	h/R	θ_c [rad]	$(\gamma_{AS} - \gamma_{LS})/\gamma_{AL}$	d/R
Bare glass (N)	0.40	0.76	0.72	
Bare glass (N_{TB})	0.42	0.79	0.70	0.43
PVA (N)	0.25	0.49	0.88	
PVA (N_{TB})	0.30	0.58	0.83	0.32
JALS204 (N)	0.62	1.11	0.45	
JALS204 (N_{TB})	0.63	1.12	0.43	

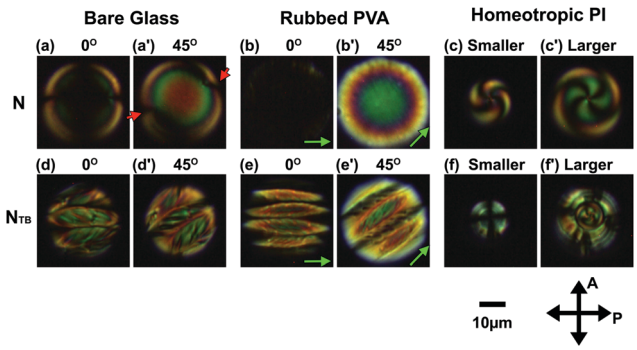

Fig. 2 Polarization micrographs of spherical-cap droplets in (a–c, a′–c′) N ($T \sim 90$ °C) and (d–f, d′–f′) N_{TB} ($T \sim 60$ °C) phases, placed on three different substrates, (a, a′, d, d′) bare glass, (b, b′, e, e′) rubbed PVA, and (c, c′, f, f′) homeotropic PI. Scale bar, 10 μm. The green arrows in the rubbed PVA results represent the rubbing direction. Each image set of (a, a′), (b, b′), (d, d′), and (e, e′) was taken for the same droplet but with two different rotation angles, (a, b, d, e) 0° (extinction) and (a′, b′, d′, e′) 45° (bright state). The N_{TB} states (d, d′, e, e′, f, f′) are obtained by cooling from (a, a′, b, b′, c, c′), respectively. Note that the droplets (c, f) and (c′, f′) are different, specifically, (c, f) small, and (c′, f′) large droplets.

III. Textures

A. Temperature and surface treatment dependence

Fig. 2 shows POM micrographs as viewed from the top of the spherical-cap droplets in N and N_{TB} phases on the three types of substrates. The N droplets on the bare glass have a 'bipolar'-type texture (Fig. 2(a) and (a′)) with two defect points. Extinction occurs for every 90° rotation of the sample indicating a uniform director field for each droplet, although its azimuthal director angle changes randomly by every cycle of heating and cooling between Iso and N. Similar concentric colours are observed for the N droplets on the rubbed PVA (Fig. 2(b) and (b′)), although the defect points are not observed as those formed in the N droplets on bare glass. Again, extinction is confirmed for every 90° rotation of the sample, implying a unidirectional alignment. However, the director in this case is always aligned to the rubbing direction indicated by green arrows. On homeotropic PI substrates a spiraling extinction cross appears in the N phase (Fig. 2(c) and (c′)). Note that the spiraling direction is not given uniquely, *i.e.* the handedness may change after melting. This fact confirms that the whole system is achiral, and the swirling pattern is not due to an intrinsic chirality.

In all cases, the textures alter on cooling through the N to N_{TB} phase transition. For both bare glass (Fig. 2(d) and (d′)) and rubbed PVA (Fig. 2(e) and (e′)), the stripe domains are decorated with a shorter periodicity stripe pattern. The direction of the boundaries of these stripe domains corresponds to the N director, *i.e.*, in the case of the rubbed PVA, it is parallel to the rubbing direction. Such stripe domains have also been observed in N_{TB} LC confined to sandwich cells or smectic A shells with planar anchoring, and they are described as the periodic modulation of the layer structures.[12,13,31,32,43,49,54] Thus, we can expect that the appearance of the stripes in the present system should also be described by such layer modulation. For the homeotropic PI, a simple SmA type extinction cross is observed for relatively small droplets (Fig. 2(f)), which becomes more complicated in larger

droplets, showing two distinguishable inner and outer regions (Fig. 2(f′)). A circular domain with a swirling cross appears in the inner region resembling the N droplet on homeotropic PI, while the outer region shows a non-twisted extinction cross with SmA-type fan-shaped domains. Since Fig. 2(f′) was observed at about 10 degrees below the N–N_{TB} transition, it is unlikely that the textural difference between the inner and the outer regions is related to the temperature inhomogeneity of the N–N_{TB} transition. Therefore we conclude the N and N_{TB}-like textures coexist despite the entire droplet is in the N_{TB} phase. To the best of our knowledge, such situation has never been observed in the SmA phase of simple layered structure.

B. Photo-induced transition

As reported earlier, UV irradiation to CB6OABOBu induces a reversible transition from N_{TB} to N, due to the *cis*-to-*trans* isomerization of the azo-benzene causing conformational change that makes the molecular shape incompatible with the local packing requirement in N_{TB}.[55] Textural changes could be induced also in our mixtures using 0.6 mW intensity light. Specifically, we found that the stripe domains formed in the N_{TB} droplets on bare glass and rubbed PVA could be erased using UV (see Fig. 3(a) and (b)) and re-appeared after the UV was turned off, (Fig. 3(a′), (b′) and Movies S1(a)–(d) in ESI1†). This phenomenon can be understood as a result of the reversible photo-induced transitions between N_{TB} and N.

The UV-induced textural changes for larger droplets on non-rubbed PI is more complex. First the outer SmA-type domains melt into a smooth N-type texture, while the inner region remains unchanged (see Fig. 3(c) and Movie S1(e) in ESI1†). Further UV irradiation completes the transition process with the transformation in the inner region, so the entire droplet became almost identical to the N droplet with a spiraling cross. When the UV irradiation is switched off, spiraling fringes appear first, as shown in Fig. 3(c′) and Movie S1(f) in ESI1.† This fringe state persists for a few seconds, and then the inner circular region re-appears to restore the initial focal-conic state of the N_{TB} droplet.

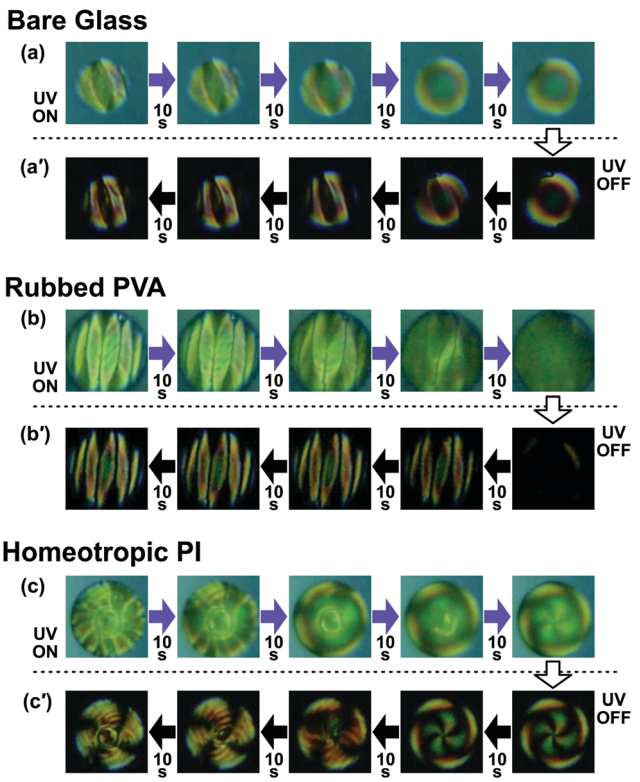

Fig. 3 Temporal texture change of N_{TB} droplets undergoing photo-induced transition, on (a, a′) bare glass, (b, b′) rubbed PVA, and (c, c′) homeotropic PI substrates. Temperature was stationary at ~60 °C. (a, b, c) The changes with time after switching on UV, and (a′, b′, c′) after switching off UV. Time intervals are given between the images. See also the corresponding movies available in ESI1.†

IV. Structural properties

A. N droplet structure

1. On bare glass. As described earlier, on bare glass the N droplets show 'bipolar'-type textures (Fig. 2(a) and (a′)) often observed in spherical N droplets surrounded by a surface with planar anchoring.[1–3] However, in the present case, two apparent defects are not located at the edge, but slightly inside the droplet. By rotating the sample by 45°, two-fold brushes corresponding to s = +1/2 defects are observed (see red arrow in Fig. 2(a′)), unlike the usual 'bipolar' state with the defect s = +1. In addition to the crossed-polarizer condition, we conducted POM observation under the birefringence-sensitive state using a tint plate to visualize even slight deformations in the director field. As shown in Fig. 4(a), very slight colour deviation from purple to blue or yellow (the blue and orange ellipses) can be seen in the edge regions at ±45° with respect to the polariser direction. Thus, this observation confirms the existence of a slight deformation of the director field due to the planar anchoring and the curvature of the air–LC interface. Since blue and yellow correspond to additive and reductive birefringence colours according to the Michel–Levi chart, respectively, the director configuration is identified as indicated by the yellow and blue ellipses in Fig. 4(a). It should be noted here that this anchoring condition is the opposite from that in a conventional calamitic LC, such as 5CB. We return to this unusual observation at the end of Section IV-A3.

Based on these observations, it is clear that the circular N director field is tangential along the droplet edge. Hence, two s = +1/2 line defects appear slightly inside, instead of the s = +1 point defects at the edge as drawn in Fig. 4(b″) and (c″). This indicates that the bend deformation is more favorable than the splay deformation around the edge and the defects. This is because in bent-dimers exhibiting the N_{TB} phase the bend elastic constant is significantly smaller than the splay and twist elastic constants.[39–42] In the present case, the bend deformation along the round edge and the s = +1/2 defects are preferred over the more costly vertical splay at the edge and the splay around the s = +1 defects (see also ESI3†). In addition, in the present system, the azimuthal anchoring on the bare glass substrate

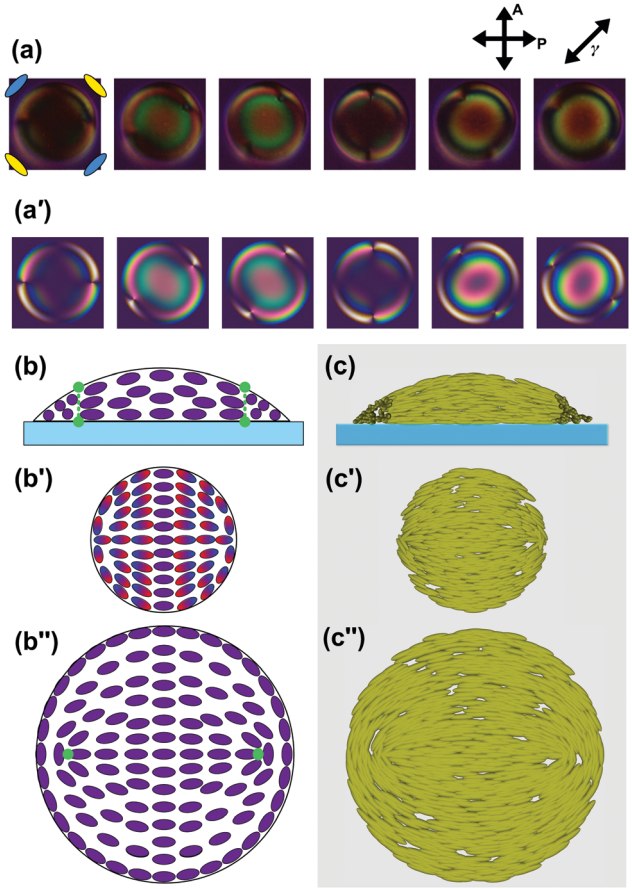

Fig. 4 Structural analysis for N droplet on bare glass. (a) POM observed with a tint plate. The directions of polarisers and the optic axis of the tint plate are shown together. The blue and yellow ellipses in the leftmost figure represent molecular orientations deduced from the colour change at the edges in these directions. (a′) Simulation result using the Jones matrix method. The calculation was done with the director field described by eqn (2). (b and b′) Schematic representation of the director field deduced from the experimental and simulation results. (b) sideview cross-section at the centre, and top-view cross-sections (b′) at the mid-plane and (b″) in the vicinity of the substrate. The ellipses show the point-by-point distributions of the N directors projected onto the plane. A pair of line defects exist in the droplet as shown by the green lines in (b) and symbols in (b″). Only focusing on the droplet surface, we can find 4 point defects with s = +1/2 (symbols in (b)), which satisfy the conservation law of topological charge under planar anchoring condition.[19] The colour gradation of these ellipses from red to blue represents the director tilt from up to down against the plane. (c–c″) Computer-generated 3D cartoons based on eqn (2) for the cross-sections corresponding to (b–b″), respectively.

should be sufficiently weak for the director to follow the circular edge alignment. Although these two line defects repel each other, they are also pushed inside by the edge. Thus, the defect positions are determined by the balance of these repulsive forces. Such a change of the defect shape from the point to line has also been observed in spherical nematic droplets under the planar anchoring condition with relatively low bend elastic constant.[3,5] However, in this case one defect line is formed at the central axis of the droplet with s = +1, different from our result. Although in both cases the appearance of the line defect is attributed to the low bend elastic constant, the selection mechanism for the one +1 or two +1/2 defects is missing. For the determination, further detailed experiments and theoretical modelling would be necessary, which are beyond the scope of this paper. According to the above considerations, the director field was approximated by the following trial functions (see also ESI2†),

$$n_r = \cos\left(\frac{\alpha z r \cos(\phi-\phi_0)}{hR}\right)\cos(\phi-\phi_0-\phi_n)$$
$$n_\phi = -\cos\left(\frac{\alpha z r \cos(\phi-\phi_0)}{hR}\right)\sin(\phi-\phi_0-\phi_n) \quad (2)$$
$$n_z = \sin\left(\frac{\alpha z r \cos(\phi-\phi_0)}{hR}\right),$$

where

$$\phi_n = \begin{cases} -\phi_p/2 & \text{for } (0<\phi-\phi_0<\pi) \\ \phi_p/2 & \text{for } (-\pi<\phi-\phi_0<0) \end{cases}$$

$$\phi_p = \begin{cases} -\arctan\zeta_+ & \text{for } (\pi/2<\phi-\phi_0<\pi) \\ \arctan\zeta_+ & \text{for } (0<\phi-\phi_0<\pi/2) \\ \arctan\zeta_- & \text{for } (-\pi/2<\phi-\phi_0<0) \\ -\arctan\zeta_- & \text{for } (-\pi<\phi-\phi_0<-\pi/2) \end{cases}$$

$$\zeta_\pm = \frac{r\cos(\phi-\phi_0)\sin\phi_d}{r\sin(\phi-\phi_0)\sin\phi_d \mp R_d\cos\phi_d}$$

$$\phi_d = \begin{cases} \arctan\xi & \text{for } (0<\phi-\phi_0<\pi) \\ -\arctan\xi & \text{for } (-\pi<\phi-\phi_0<0) \end{cases}$$

$$\xi = \frac{2rR_d\sin(\phi-\phi_0)}{r^2-R_d^2}.$$

For this model structure the range of the parameters should be set as,

$$0<\phi_p,\quad \phi_d<\pi \quad \text{for } (0<\phi-\phi_0<\pi)$$

$$-\pi<\phi_p,\quad \phi_d<0 \quad \text{for } (-\pi<\phi-\phi_0<0).$$

Here, the cylindrical coordinate system is set at the substrate plane in such a way that the z-axis is perpendicular to the substrate. ϕ_0 and R_d correspond to the azimuthal angle of the direction connecting two s = +1/2 defects and the midway distance between them, respectively. Finally, α is a dimensionless parameter. To validate this structural model, we simulated the spatial distribution of the light transmission intensity between crossed polarizers using the Jones matrix method. The simulated POMs (Fig. 4(a′)) are compared with the experimental observations (Fig. 4(a)). Apparently, even detailed features of the birefringent colours are reproduced, particularly those around the defect points, validating our structural model. We would like to emphasize that this s = +1/2 defect structure is unique to the present system characterized by the small bend elastic constant,

and planar anchoring at the LC–air and the LC–substrate interfaces.

2. Rubbed-PVA. Unlike on the bare glass substrate, the director at the surface of the rubbed PVA is strongly anchored and aligned almost unidirectionally along the rubbing direction (Fig. 2(b) and (b′)). Fig. 5(a) shows the POM textures captured with the tint plate. Again, blue and orange colours are observed at the edge regions, which means the director field is deformed along the round edge. Since uniform alignment is achieved only in the vicinity of the LC–substrate interface, the director is continuously deformed towards the LC–air interface with strong planar anchoring which forces the director to be aligned along the curved LC–air interface. The small contact angle (high wettability, see Table 1) with respect to the substrate may reduce the vertical splay at the edge, therefore the system can accept and maintain the 'bipolar' state more likely than on bare glasses. Based on these observations, the director field is assumed to be as shown in the cartoons in Fig. 5(b), (b″) and (c), (c″). The only concern with this model is that no defect is observed in POM, although such a confined state with a closed boundary of planar anchoring topologically requires defects. We think that this is due to the weak anchoring at the air–LC interface, which allows the director to be not entirely along the surface. The essential difference between this and the case of the bare substrate, where the defect lines are induced, is in the nature of the planar anchoring: the PVA-coated substrate align the director unidirectionally, while the bare glass cannot align the azimuthal angle of the director on the substrate. Therefore, the director can deform on the bare glass in contrast to the rubbed PVA substrate. This difference in the azimuthal anchoring results in the +1/2 line defects on the bare glass and the small splay deformation with no defect on the PVA-coated substrate.

In the PVA-coated substrate, the director field can be approximated as (see also ESI2†),

$$n_r = \cos\left(\frac{\alpha z r \cos(\phi-\phi_0)}{hR}\right)\cos\left(\phi-\phi_0+\frac{\beta z r^2 \sin 2(\phi-\phi_0)}{2hR^2}\right)$$
$$n_\phi = -\cos\left(\frac{\alpha z r \cos(\phi-\phi_0)}{hR}\right)\sin\left(\phi-\phi_0+\frac{\beta z r^2 \sin 2(\phi-\phi_0)}{2hR^2}\right)$$
$$n_z = \sin\left(\frac{\alpha z r \cos(\phi-\phi_0)}{hR}\right). \quad (3)$$

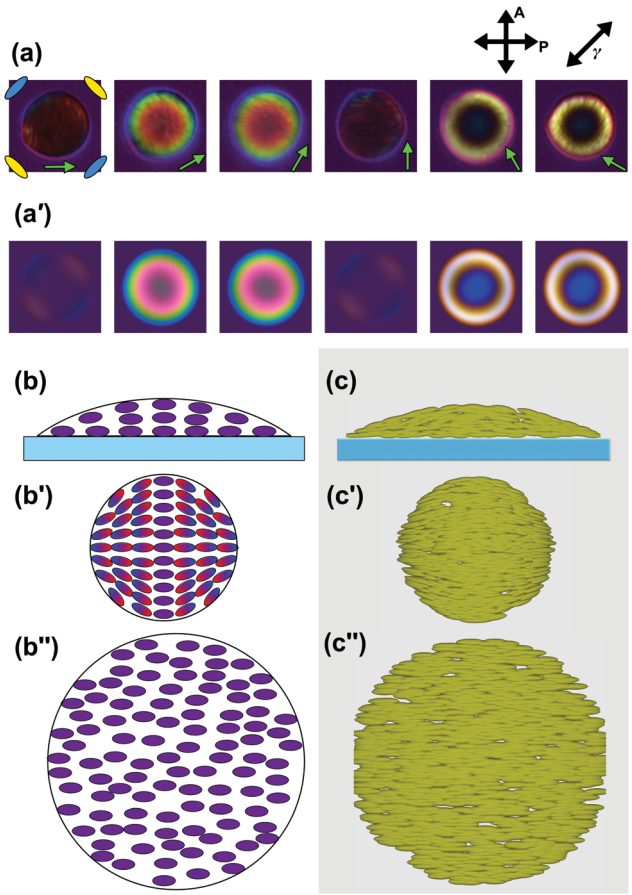

Fig. 5 Structural analysis for N droplet on PVA-coated glass based on eqn (3). See the caption of Fig. 4 for explanation of (a and a′), (b–b″) and (c–c″).

The coordinates and the parameters are defined similarly to eqn (2), except for the non-dimensional parameter β. The director field given by eqn (3) does not have defects, and the simulated POM images perfectly reproduce the experimental POMs, *cf.* Fig. 5(a) and (a′). In this case, the strong unidirectional anchoring of the rubbed PVA surface retains the splay deformations at the edge whereas in the case of bare glass with weak anchoring, the director escapes from the splay into the bend around the $s = +1/2$ line defects (see also ESI3†).

The total free energy for the director field of eqn (3) can be calculated, and from the result, the anchoring constant at air–LC interface is estimated to be $W_{air} \sim 10^{-6}$–10^{-8} N m^{-1} as described in ESI4.† In addition, the anchoring constant of PVA is reported to be $W_{PVA} \sim 10^{-5}$ N m^{-1} in ref. 62. Thus, W_{PVA} is 1–3 order larger than W_{air}, which consists with the above discussion.

More generally, in all of the present N droplets in this manuscript, the elastic free energy in bulk and anchoring energy at air–LC interface can be roughly estimated. Assuming the elastic constant is $K \sim 10^{-11}$–10^{-12} N[63] and the droplet radius $R \sim 10^{-5}$ m, the energies are given as $F_d \sim KR \sim 10^{-16}$–$10^{-17}$ J and $F_a \sim WR^2 \sim 10^{-16}$–$10^{-18}$ J, respectively. These show comparable values with each other, which indicates that the director deformation would be induced by the anchoring at air–LC interface.

3. Homeotropic PI. In contrast to the two previous cases in which both the LC–air and the LC–substrate interfaces have planar anchoring, here the LC–substrate interface has homeotropic anchoring, while the LC–air interface maintains planar anchoring. In such a case the director field is generally considered to become conically symmetric (Fig. S5(a) in ESI5†), and the resulting texture has the so-called 'Maltese-cross' pattern. However, the actual POM texture shows a spiralling pattern (Fig. 2(c) and (c′)), indicating a

twisted director field, as described by the trial functions (see also ESI2†),

$$n_r = -\sin\left(\frac{\pi z}{2h}\right)\cos\left(\frac{\beta(R-r)}{R}\right)$$
$$n_\phi = -\sin\left(\frac{\pi z}{2h}\right)\sin\left(\frac{\beta(R-r)}{R}\right) \quad (4)$$
$$n_z = -\cos\left(\frac{\pi z}{2h}\right).$$

Again, the coordinates and the parameters are defined similarly to the cases for eqn (2) and (3). It should be noted that β is a parameter for the twist deformation along the radial direction, and $\beta = 0$ gives a conical director structure with a splay deformation as illustrated in Fig. S1 in ESI2.† However, when β takes non-zero values, the twist deformation is induced along the radial direction, by which the bend deformation is partially replaced by splay. Finally, $\beta = \pm\pi/2$ gives a ring-like director field with the bend around the central axis of the droplet, while the splay deformation is maintained at the edge region as shown in Fig. 6(b′) and (c′) (see also ESI3†). The simulated POM image with $\beta = \pi/2$ in Fig. 6(a′) agrees well with the real image shown in Fig. 6(a). This structure is also energetically favored because the bend elastic constant is the smallest.[39–42] The escape from the splay to a bend and twist dominant structure leads to the spiral structure. In fact, such a director twist has also been reported in the achiral N droplets with low twist or bend elastic constants.[6–10]

In contrast to the present case, conventional NLCs, such as 5CB, show line defects only with planar anchoring at the substrate and homeotropic anchoring at the LC–air interface.[16] The difference between the anchoring properties at the LC–air interface of conventional NLCs and the present dimer, presumably reflects differences in their respective structural. Thus the unusual planar anchoring at the air interface for the dimer is probably due to the placement of the flexible hydrocarbon chains in the center of the molecule instead of at the end as in conventional LCs. For entropy reasons the alkyl chains prefer to be in contact with air, inducing homeotropic alignment in 5CB and planar for CB6OABOBu.

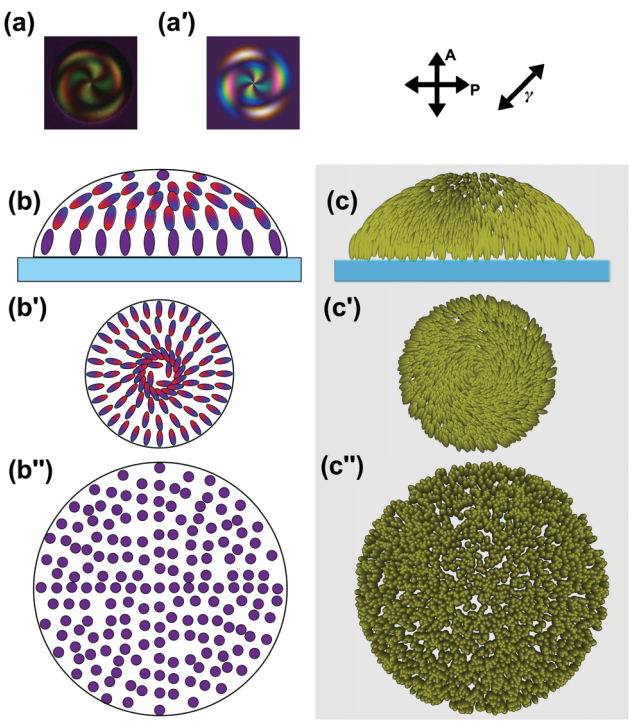

Fig. 6 Structural analysis for N droplet on homeotropic PI-coated glass. Also see the caption of Fig. 4.

B. Structures of N_{TB} droplets

As described earlier, the N_{TB} droplets on the bare glass and the rubbed PVA substrates show stripes decorated with zigzag undulations. Such stripes and undulations are often observed in smectic A (SmA) shells with finite thickness[12,13,31,32] and for the N_{TB} phase in sandwich cells with planar anchoring conditions.[43,49,54] In smectics, the requirement for the constant layer spacing prohibits the bend deformation.[63] Therefore, frustration occurs in the spherical shells with planar anchoring, often resulting in the periodic buckling of the layered structure.[12,13,21,22] Similarly, the nanoscale heliconical arrangement of the N_{TB} phase is considered as a pseudo-layer structure, so that the constraints imposed by the curved surface with planar anchoring trigger the buckling instability of the pseudo-layers.[49,54] Since the pseudo-layers may shrink on cooling, this can also trigger the periodic buckling (Fig. 7(a)).

Previous studies of SmA and N_{TB} LCs showed that the stripe period increases with sample thickness.[31,43] In Fig. 7(b) we plot the stripe period d and the droplet height h as a function of the droplet radius R. Both for the bare glass and the rubbed PVA, d and h are proportional to R and are almost equal. This reinforces the view that the formation of the stripe pattern in our N_{TB} droplets may be described using a similar mechanism to that for the stripes formed in the SmA shells or by the N_{TB} LC in sandwich cells.

Fig. 2(f) shows that smaller N_{TB} droplets on homeotropic PI appear similar to circular domains of Sm LCs, emphasizing the pseudo-layer nature of the nanoscale heliconical structure of the N_{TB} phase. Larger N_{TB} droplets however have different structures in the inner and outer regions as shown in Fig. 2(f′). This structure is different from the bunch structures of radially-arranged focal-conics of Sm droplets reported previously.[32–36] The striped texture of the outer region can be understood as a consequence of the N_{TB} pseudo-layer structure. The texture of the circular inner domain however is similar to that we found in the N phase (see Fig. 2(c′)). The inner circular region seems to have a distinct size variation on the droplet radius (R) and droplet height (h) as shown in Fig. 7(c). Similar to the case of the planar anchoring, h shows linear dependence on R (purple dots) although with a steeper slope due to the larger contact angle (see Table 1). However, R_c, being a few times smaller than the droplet height h (red squares), shows a non-linear dependence on R. From the texture, we qualitatively model a plausible structure as sketched in Fig. S3(a) in ESI3,† in which the droplet consists of three regions, Regions I–III. Region I is the outermost part containing stripes. Here, the pseudo-layers are considered to be bent and the helical axis of which is splayed to

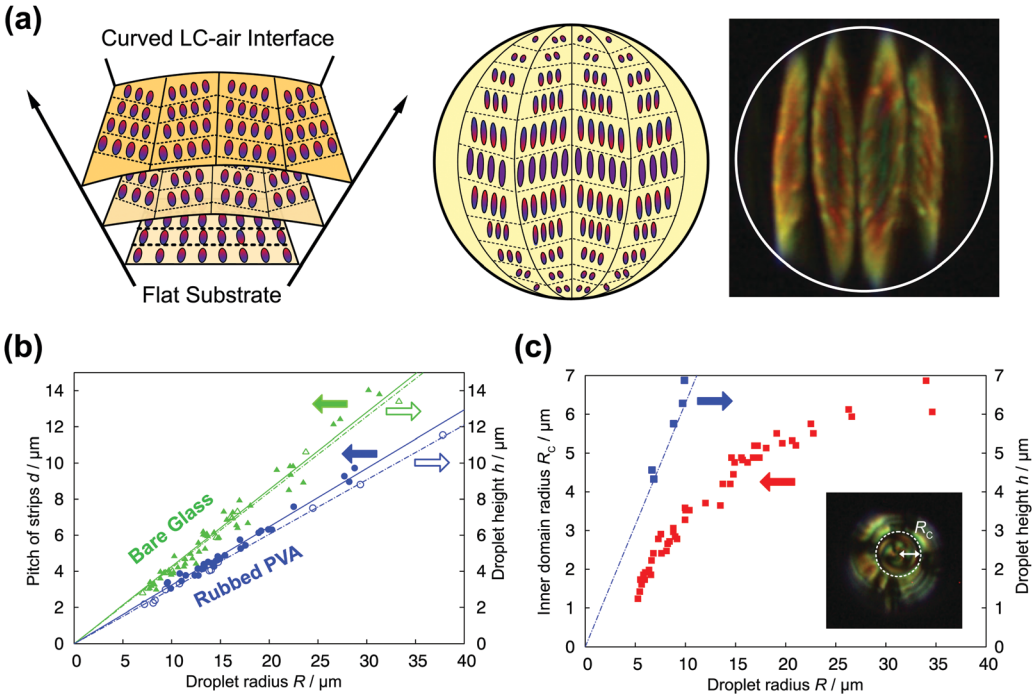

Fig. 7 (a) A model for the stripe domains of the spherical-cap N_{TB} droplets on the bare glass and the rubbed PVA substrates. In this model, pseudo-layer nature of nano-pitched helix is the cause of the stripes and undulations. This model is borrowed from ref. 13, made for the similar structure with layer undulations in thick smectic shells. Dotted lines show the direction of the pseudo-layers. See the caption of Fig. 4–6 for the explanation of the ellipses. (b) The pitch of stripes d and the droplet height h plotted against the droplet radius R. The measurement was performed at ~60 °C. In all the cases, the data are well fitted by linear functions, and interestingly d coincides with h. The slope values d/R and h/R are summarized in Table 1. (c) The R dependence of the radius (R_c) of the inner circular domain appearing in the large spherical-cap N_{TB} droplet on the homeotropic PI. The measurement was performed at ~60 °C. The corresponding droplet height h is also plotted. In the whole R range, R_c is smaller than h, and it shows a non-linear dependence with the droplet radius.

connect the planar alignment at the air interface and the homeotropic alignment at the substrate. The stripes are a result of the buckling of the pseudo layers due to the decrease of the pitch on cooling. Region II is the cylindrical part in the inner region, surrounded by Region I. Region II also has pseudo-layers but parallel to the substrate, and thus no deformation of the pseudo-layers to cost the deformation free energy. This region can avoid buckling by changing its radius to compensate for the pitch variation on cooling. Region III is the spherical-cap part on the top of Region II, whose height is estimated to be several hundreds of nanometers (for more details of this estimation, see ESI6†). Since this region is a thin layer sandwiched between two different boundaries of homeotropic and planar alignment conditions, strong geometrical frustration occurs. As a result, Region III melts into nematic ordering without the twist-bend structure. Since Region II is optically isotropic and hence does not contribute to the birefringence colour, the texture of the inner part reflects only the features of Region III. Therefore, it looks like a nematic droplet embedded in the center. Note that smaller droplets only consist of Region I.

V. Summary

In this paper, we prepared spherical-cap droplets on glass substrates exposed to the air using the photo-responsive bent-shaped dimer CB6OABOBu which shows the N and N_{TB} phases. In the droplets, the switching of these two phases was successfully performed using a change in temperature or by UV light irradiation. In addition, to control the structure inside the droplets, we prepared three types of the substrates: bare, PVA-coated and homeotropic PI-coated glasses.

Structures in the N droplets are different from those seen for conventional calamitic nematic droplets due to the anomalously low director bend elastic constant of bent dimers. POM observations of the N droplets revealed that the anchoring condition at the air–LC interface is a planar alignment in contrast to the homeotropic alignment typical for calamitic nematics, such as 5CB. On bare glass and PVA coated substrates, 'bipolar'-type structures are formed in the droplets. However, the detailed structures were different for these two cases: on the bare glass substrate, a pair of +1/2 line defects formed inside the droplet to avoid the splay and induce bend deformation, while on the PVA-coated substrate, the defects are not formed but slight director deformations were induced at the edge, owing to the strong planar anchoring and the low contact angle. On the homeotropic PI, despite the absence of molecular chirality, a twisted director field with a spiraling Maltese cross formed, as this structure minimized the costly splay deformations.

In the N_{TB} droplets, the structures were more complex. On bare and PVA-coated substrates, a stripe pattern with a period d of several to several tens of micrometres was observed.

This pattern formation may be explained by the periodic buckling of the pseudo-layers of the N_{TB} phase due to geometrical frustration induced by the surface with planar anchoring, by analogy with spherical SmA shells or N_{TB} LC in sandwich cells. On homeotropic PI, a SmA-like fan-shaped texture was observed for smaller droplets. For larger droplets, a circular domain of several micrometers with a N-like smooth texture at its centre appeared. We proposed a structural model that can qualitatively explain the formation of this nematic-like inner region.

Conflicts of interest

There are no conflicts to declare.

Acknowledgements

The stays and research activities of J. Y. and F. A. in Hungary, and P. S. and A. B. in Japan are supported by the JSPS-HAS bilateral program. J. Y. was partially supported by JSPS KAKENHI Grant Number 15K17739. A. J. acknowledges financial support by NSF DMR: 1307674. Financial support from the grants NKFIH PD 121019 and FK 125134 are acknowledged.

References

1 M. Candau, P. LeRoy and F. Debeauvais, *Mol. Cryst. Liq. Cryst.*, 1973, **23**, 283.
2 G. E. Volovik and O. D. Lavrentovich, *Sov. Phys. JETP*, 1983, **58**, 1159.
3 P. Drzaic, *Mol. Cryst. Liq. Cryst.*, 1988, **154**, 289.
4 R. OndrisCrawford, E. P. Boyko, B. G. Wagner, J. H. Erdmann, S. Zumer and J. William Doane, *J. Appl. Phys.*, 1991, **69**, 6380.
5 J. Jiang and D.-K. Yang, *Liq. Cryst.*, 2018, **45**, 102.
6 A. Rüdinger and H. Stark, *Liq. Cryst.*, 1999, **26**, 753.
7 K.-U. Jeong, D.-K. Yang, M. J. Graham, Y. Tu, S.-W. Kuo, B. S. Knapp, F. W. Harris and S. Z. D. Cheng, *Adv. Mater.*, 2006, **18**, 3229.
8 D.-K. Yang, K.-U. Jeong and S. Z. D. Cheng, *J. Phys. Chem. B*, 2008, **112**, 1358.
9 J. Jeong, Z. S. Davidson, P. J. Collingsa, T. C. Lubensky and A. G. Yodh, *Proc. Natl. Acad. Sci. U. S. A.*, 2014, **111**, 1742.
10 J. Ignés-Mullol, G. Poy and P. Oswald, *Phys. Rev. Lett.*, 2016, **117**, 057801.
11 A. Fernández-Nieves, V. Vitelli, S. Utada, D. R. Link, M. Márquez, D. R. Nelson and D. A. Weitz, *Phys. Rev. Lett.*, 2007, **99**, 157801.
12 H.-L. Liang, S. Schymura, P. Rudquist and J. Lagerwall, *Phys. Rev. Lett.*, 2011, **106**, 247801.
13 T. Lopez-Leon, A. Fernández-Nieves, M. Nobili and C. Blanc, *Phys. Rev. Lett.*, 2011, **106**, 247802.
14 H.-L. Liang, R. Zentel, P. Rudquistc and J. Lagerwall, *Soft Matter*, 2012, **8**, 5443.
15 M. D. Kleman and O. D. Lavrentovich, *Philos. Mag.*, 2006, **86**, 4117.
16 V. K. Gupta and N. L. Abbot, *Langmuir*, 1999, **15**, 7213.
17 O. Mondain-Monval, J. C. Dedieu, T. Gulik-Krzywicki and P. Poulin, *Eur. Phys. J. B*, 1999, **12**, 167.
18 Y. Gu and N. L. Abbott, *Phys. Rev. Lett.*, 2000, **85**, 4719.
19 M. Tasinkevych, N. M. Silvestre and M. M. T. da Gama, *New J. Phys.*, 2012, **19**, 073730.
20 J. Yoshioka, F. Ito and Y. Tabe, *Soft Matter*, 2016, **12**, 2400.
21 F. Ito, J. Yoshioka and Y. Tabe, *J. Phys. Soc. Jpn.*, 2016, **85**, 114601.
22 G. Poy, F. Bunel and P. Oswald, *Phys. Rev. E*, 2017, **96**, 012705.
23 F. Xu and P. P. Crooker, *Phys. Rev. E*, 1997, **56**, 6853.
24 D. Seč, T. Porenta, M. Ravnik and S. Žumer, *Soft Matter*, 2012, **8**, 11982.
25 D. Seč, S. Čoper and S. Žumer, *Nat. Commun.*, 2014, **5**, 3057.
26 T. Orlova, S. J. Aßhoff, T. Yamaguchi, N. Katsonis and E. Brasselet, *Nat. Commun.*, 2015, **6**, 7603.
27 G. Posnjak, S. Čoper and I. Muševič, *Sci. Rep.*, 2016, **6**, 26361.
28 G. Posnjak, S. Čoper and I. Muševič, *Nat. Commun.*, 2017, **8**, 14594.
29 M. K. Krakhalev, A. P. Gardymova, O. O. Prishchepa, V. Y. Rudyak, A. V. Emelyanenko, J.-H. Liu and V. Y. Zyryanov, *Sci. Rep.*, 2017, **7**, 14582.
30 J. Yoshioka and F. Araoka, *Nat. Commun.*, 2018, **9**, 432.
31 O. V. Manyuhina and M. J. Bowick, *J. Non-Linear Mech.*, 2015, **75**, 87.
32 G. Lee, F. Araoka, K. Ishikawa, Y. Momoi, O. Haba, K. Yonetake and H. Takezoe, *Part. Part. Syst. Charact.*, 2013, **30**, 847.
33 H. Naito, M. Okuda and O.-Y. Zhong-can, *Phys. Rev. E: Stat. Phys., Plasmas, Fluids, Relat. Interdiscip. Top.*, 1995, **52**, 2095.
34 C. Meyer, L. L. Cunff, M. Belloul and G. Foyart, *Materials*, 2009, **2**, 499.
35 M. A. Gharbi, I. B. Liu, Y. Luo, F. Serra, N. D. Bade, H.-N. Kim, Y. Xia, R. D. Kamien, S. Yang and K. J. Stebe, *Langmuir*, 2015, **31**, 11135.
36 D. A. Beller, M. A. Gharbi, A. Honglawan, K. J. Stebe, S. Yang and R. D. Kamien, *Phys. Rev. X*, 2013, **3**, 041026.
37 P. Oswald and P. Pieranski, *Smectic and Columnar Liquid Crystals*, CRC Press, Boca Raton, 2006.
38 I. Dozov, *Europhys. Lett.*, 2001, **56**, 247.
39 V. Borshch, *et al.*, *Nat. Commun.*, 2013, **4**, 2635.
40 C.-J. Yun, M. R. Vengatesan, J. K. Vij and J.-K. Song, *Appl. Phys. Lett.*, 2015, **106**, 173102.
41 N. Sebastián, *et al.*, *Phys. Chem. Chem. Phys.*, 2016, **18**, 19299.
42 K. Adlem, M. Čopič, G. R. Luckhurst, A. Mertelj, O. Parri, R. M. Richardson, B. D. Snow, B. A. Timimi, R. P. Tuffin and D. Wilkes, *Phys. Rev. E: Stat. Phys., Plasmas, Fluids, Relat. Interdiscip. Top.*, 2013, **88**, 22503.
43 V. P. Panov, *et al.*, *Phys. Rev. Lett.*, 2010, **105**, 167801.
44 D. Chen, *et al.*, *Proc. Natl. Acad. Sci. U. S. A.*, 2013, **110**, 15931.
45 C. Meyer, G. R. Luckhurst and I. Dozov, *Phys. Rev. Lett.*, 2013, **111**, 067801.
46 S. M. Shamid, S. Dhakal and J. V. Selinger, *Phys. Rev. E: Stat., Nonlinear, Soft Matter Phys.*, 2013, **87**, 052503.
47 R. Balachandran, V. P. Panov, Y. P. Panarin, J. K. Vij, M. G. Tamba, G. H. Mehl and J. K. Song, *J. Mater. Chem. C*, 2014, **2**, 8179.

48 C. Greco, G. R. Luckhurst and A. Ferrarini, *Soft Matter*, 2014, **10**, 9318.
49 P. K. Challa, V. Borshch, O. Parri, C. T. Imrie, S. N. Sprunt, J. T. Gleeson, O. D. Lavrentovich and A. Jákli, *Phys. Rev. E: Stat., Nonlinear, Soft Matter Phys.*, 2014, **89**, 060501.
50 E. Gorecka, N. Vaupotič, A. Zep, D. Pociecha, J. Yoshioka, J. Yamamoto and H. Takezoe, *Angew. Chem.*, 2015, **54**, 10155.
51 M. R. Tuchband, *et al.*, 2015, arXiv:1511.07523.
52 Z. Parsouzi, *et al.*, *Phys. Rev. X*, 2016, **6**, 021041.
53 C. Meyer and I. Dozov, *Soft Matter*, 2016, **12**, 574.
54 N. Vaupotič, A. Ali, P. W. Majewski, E. Gorecka and D. Poiecha, *Chem. Phys. Chem.*, 2018, **19**, 2566.
55 D. A. Paterson, *et al.*, *J. Am. Chem. Soc.*, 2016, **138**, 5283.
56 K. S. Krishnamurthy, P. Kumar, N. B. Palakurthy, C. V. Yelamaggada and E. G. Virga, *Soft Matter*, 2016, **12**, 4967.
57 C. Meyer, D. Stoenescu, G. R. Luckhurst, P. Davidson and I. Dozov, *Liq. Cryst.*, 2017, **44**, 232.
58 R. C. Jones, *J. Opt. Soc. Am.*, 1941, **31**, 488.
59 N. A. Vaz and G. P. Montgomery, *J. Appl. Phys.*, 1987, **62**, 3161.
60 M. Kleman and O. D. Lavrentovich, *Soft Matter Physics An Introduction*, Springer, New York, 2003.
61 M.-W. Yang and S.-Y. Lin, *Colloids Surf., A*, 2003, **220**, 199.
62 M. M. Wittebrood, T. Rasing, S. Stallinga and I. Muševič, *Phys. Rev. Lett.*, 1998, **80**, 1232.
63 P. G. de Gennes and J. Prost, *The Physics of Liquid Crystals second edition*, Clarendon Press, Oxford, New York, 1993.

